A thin-film broadband perfect absorber based on plasmonic copper nanoparticles

Nanda Perdana [a,*], Jonas Drewes [b], Felix Pohl [b], Alexander Vahl [b], Thomas Strunskus [b], Mady Elbahri [c], Carsten Rockstuhl [a,d], Franz Faupel [b]

[a] Institute of Theoretical Solid State Physics, Karlsruhe Institute of Technology (KIT), Karlsruhe 76137, Germany
[b] Institute of Material Science, Chair for Multicomponent Materials, Kiel University, Kiel 24143, Germany
[c] Nanochemistry and Nanoengineering, School of Chemical Engineering, Department of Chemistry and Materials Science, Aalto University, Aalto 00076, Finland
[d] Institute of Nanotechnology, Karlsruhe Institute of Technology (KIT), Karlsruhe 76021, Germany

ARTICLE INFO

ABSTRACT

Increasing the efficiency of solar thermal collectors is extremely important as they are essential for many applications, ranging from the UV up to the NIR spectral range, from water heating systems up to microelectromechanical systems. In this work, a plasmonic multilayer nanocomposite thin-film system that efficiently absorbs solar radiation across an extended spectral range was simulated and experimentally tested. Novel to our approach, copper nanoparticles in an alumina matrix were chosen as the nanocomposite material. Compared to other plasmonic materials such as gold or silver, copper is more abundant and economic. The alumina matrix provides high thermal stability, good optical properties, and corrosion protection. Using a multiscale-modeling approach, we inspect on computational grounds the effect of the nanoparticle filling factor, the angle of incidence, and the thin-film thicknesses on the absorber performance. We found that an optimally designed device absorbs up to 90% light energy from 200 nm to 1800 nm. To validate the simulations, two promising absorber layouts are experimentally realized. Their performance compares very well with simulations.

1. Introduction

Since the beginning of industrialization, global warming has evolved to an ever-increasing problem. The effect of global warming is severe, provoking more natural disasters [1],and diseases [2] due to climate changes, putting many human lives at risk. One of the major sources for the climate change is fossil fuel burning, as air pollution emitted by fossil energy plants worsens global warming [3]. Also, conventional oil and gas scarcity and the complex extraction process make fossil energy more expensive [4]. For these reasons, people have begun to use renewable energy, such as solar energy, since it is cheaper and cleaner compared to fossil energy. Solar energy is promising to substitute a significant share of non-renewable fossil energy within the following years [5].

Among the many options, sunlight can be collected through solar thermal collectors (STC). Such a device gathers sunlight and converts it into thermal energy, which is possibly be used directly or further converted into chemical [6] or, with compromises in terms of efficiency to electrical energy [7]. The key element of an STC is the absorber. Yet, STC's inability to absorb sunlight in a broad spectral range is the leading cause for their low efficiency [8]. It is noted that sunlight above the atmosphere and at the surface has a spectrum ranging from UV (UV) to near-infrared (NIR) wavelengths, i.e., λ = 250 nm - 2500 nm [9]. To broaden the absorption spectrum, many types of STC absorbers have been studied. Examples are a black-colored STC [10], STCs that uses mixture of materials [11–13], grating STCs [14,15], a photonic crystal STC [16], and nanoparticle arrays [17,18]. Also, there are many attempts to fabricate absorbers from plasmonic nanoparticles [19–21]. It turns out that absorbers that are based on plasmonic nanoparticles provide, in general, a strong absorption from UV to NIR spectrum while being almost polarization and angle insensitive.

This motivates their further exploration, which led to the development of dedicated multilayer systems that act as perfect broadband absorbers [22–26]. The thickness of the multilayer perfect absorber is compatible with many micro-electromechanical systems (MEMS) applications, which further promotes their exploration [27–29]. These multilayer systems can consist of a metallic ground plate, a dielectric spacer, and an absorbing layer containing the plasmonic nanoparticles. Perfect absorption can be achieved by exploiting the destructive interference of directly reflected light at the first interface from air to the absorber layer and the light that experiences multiple round trips in the cavity formed by the multilayer system. Since the ground plate prevents any transmission, light is entirely absorbed [30]. The design is appealing since it is unnecessary to consider an extended thickness for the absorbing film to reach zero reflection over a large spectral range [31]. In essence, the absorption is in spectral ranges where localized plasmons are supported in the metallic nanoparticles, but many effects can be exploited to broaden the response. For example, the probability of trapping the light between the broad-sized nanoparticles can enhance absorption [32] and this has been applied to solar-cell applications [33–37]. It also turns out later that the plasmon hybridization [38,39] can contribute to the absorption enhancement. Exploiting the hybridization allows to tune the resonance of the interacting nanoparticles in addition to choosing their shape and the material from which they are made.

So far, noble metals such as gold (Au) or silver (Ag) are commonly considered in plasmonic absorbers due to their outstanding low-loss plasmonic properties [40]. However, silver and in particular gold are scarce and the material price limits the cost efficiency of gold-nanoparticle based absorbers. Therefore, in this work, we investigate an absorber based on low-cost, less scarce materials, namely copper (Cu) nanoparticles and alumina (Al_2O_3) dielectric. We combine a computational multi-scale modeling approach to identify promising devices and afterward realize selected devices in dedicated experiments.

We begin by considering the size distribution of an experimental copper nanoparticles sample obtained with a gas aggregation source (GAS), the technique later used for the experimental realization. The details about these are explained in the experimental section. This guarantees that all the following optimizations are made within the design space experimentally accessible. We consider in the simulations initially a cluster of non-touching nanoparticles. Its electromagnetic response can be aggregated in the form of a single T-matrix. In the second step, a nanoparticle (NP) layer is created from a periodic arrangement of such nanoparticles clusters and used to compose a thin-film characterized by effective material parameters. Afterward, the perfect absorber is treated as a multilayer stack where the layer containing the nanoparticles is one of them. The optimum absorber parameters are found through parameter sweeps considering the degrees of freedom in our device. This concerns mainly the thickness of the layers for a given filling fraction. As an objective function, we seek to maximize absorption in a broad spectral range. The outcome from those analyses are blueprints for possible devices.

To validate the simulation results, two absorber designs are experimentally realized. The samples are fabricated via physical vapor deposition techniques, like RF sputtering and nanoparticle beam deposition via GAS. The alumina dielectric layer and the alumina matrix are produced via RF sputtering from an alumina target, and the nanoparticles are produced from a gas aggregation source by a DC magnetron discharge. The GAS equipped with a magnetron was firstly invented by Haberland et al. in 1992 [41]. The combination of RF sputtering and the GAS enables high purity, independent control over the filling factor, and the fabrication of nearly spherical nanoparticles without any lithography methods. This method has already been utilized successfully for fabricating Au-SiO_2 and Ag-SiO_2 thin-films with plasmonic properties [42].

We start our contribution by elaborating on the used methods. This section will be divided into two subsections. First, we overview the used computational tools. Second, we provide details on the experimental aspects. In the next section, by computational means, we explore initially the impact of several degrees of freedom on the performance of the device and conclude on promising samples that are realized and characterized. Finally, the obtained results are used to explain the nature behind the strong and broadband absorption.

2. Methods

2.1. Multi-scale modeling

We start by modeling the optical response from a cluster of homogeneous spherical nanoparticles in a cubical unit cell in an alumina background, shown in Fig. 1. The size distribution of the spherical nanoparticles was chosen according to the experimental samples, explained in the experimental method section. The size distribution considered in the simulations reproduces the details of the experimental size distribution, but only 100 nanoparticles were considered to form the cluster. This reduces the number of nanoparticles in the simulations, which simplifies the computations, while the approximated experimental size distribution is preserved. This approach guarantees that we design our devices within the parameter range accessible by the experiments. The nanoparticles are closely packed by using the force-biased algorithm for a specific filling factor (*FF*) [43]. The *FF* will be subject to a variation at a later stage. The packing assumes periodic boundary conditions so that an infinitely extended thin-film can be assembled that includes a periodic array of nanoparticles clusters to be used in later simulation steps. The spatial extension of the cluster containing 100 nanoparticles, i.e., the periodicity, depends on the desired filling factor.

The scattered field induced by an individual nanoparticle is determined through Mie theory and the T-matrix approach [44]. Mie theory tells us that the incident field $\mathbf{E}_{inc}(\boldsymbol{r})$ and the scattered field $\mathbf{E}_{sca}(\boldsymbol{r})$ from a localized particle in frequency domain can be expanded into vector spherical wave functions (VSWF) $\mathbf{M}_{mn}^{J}(\boldsymbol{r})$ and $\mathbf{N}_{mn}^{J}(\boldsymbol{r})$ as

$$\mathbf{E}_{\mathrm{inc}}(\mathbf{r}) = \sum_{n=1}^{\infty} \sum_{m=-n}^{n} p_{mn}\mathbf{N}_{mn}^{(1)}(\mathbf{r}) + q_{mn}\mathbf{M}_{mn}^{(1)}(\mathbf{r}), \tag{1}$$

$$\mathbf{E}_{\mathrm{sca}}(\mathbf{r}) = \sum_{n=1}^{\infty} \sum_{m=-n}^{n} a_{mn}\mathbf{N}_{mn}^{(3)}(\mathbf{r}) + b_{mn}\mathbf{M}_{mn}^{(3)}(\mathbf{r}) \tag{2}$$

where p_{mn}, q_{mn} are the incident and a_{mn}, b_{mn} are the scattering expansion coefficients. ω is the frequency of the field. The superscript $J = \{1, 3\}$ indicates the chosen VSWF that copes with the constraints
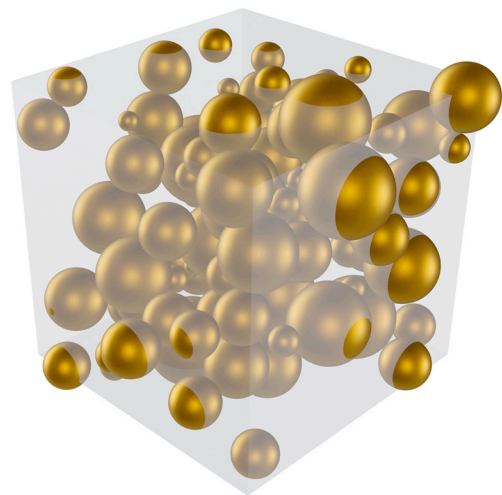

Fig. 1. A cluster of 100 nanoparticles ($FF = 33\%, \overline{d} = 12.60$ nm, $\sigma_d = 4.84$) in a cubical unit cell with lattice constant 77.25 nm.

imposed on the incident or scattered fields. While the coefficients expanding the incident field are known for a given illumination, the coefficients expanding the scattered field can be calculated through the T-matrix approach. The T-matrix $\underline{\underline{\mathbf{T}}}$ expresses the scattering properties of an object, linking the incident and the scattering expansion coefficients for a single particle, which generally reads as [45].

$$
\begin{pmatrix} a_{11} \\ \vdots \\ a_{mn} \\ b_{11} \\ \vdots \\ b_{mn} \end{pmatrix} = \underline{\underline{\mathbf{T}}} \begin{pmatrix} p_{11} \\ \vdots \\ p_{mn} \\ q_{11} \\ \vdots \\ q_{mn} \end{pmatrix}.
\tag{3}
$$

Generally, an infinite number of terms have to be retained in the expansion. However, a finite number of multipolar orders is sufficient for all practical purposes. In our case, we assume that the T-matrices of the nanoparticles have multipolar order up to the eighth. That guarantees that the calculation is converged to capture the electromagnetic coupling between the nanoparticles. Of course, the T-matrix for an isolated sphere is well known and consists of the Mie coefficients on the diagonal.

It is possible to calculate the orientation averaged extinction cross-sections C_{ext} and scattering cross-sections C_{sca} of a scatterer characterized by its T-matrix. The cross-sections are equivalent to the trace of the scatterer's T-matrix [46] defined in Eqs. (4)–(6) as

$$
C_{\text{ext}} = -\frac{2\pi}{k^2} Re \left\{ \text{Tr}\left(\underline{\underline{\mathbf{T}}}\right) \right\},
\tag{4}
$$

$$
C_{\text{sca}} = \frac{2\pi}{k^2} \text{Tr}\left(\left| \underline{\underline{\mathbf{T}}} \right|^2 \right),
\tag{5}
$$

where $k = \frac{\omega}{c}\sqrt{\epsilon_{bg}}$ is the wavenumber in the background medium. The absorption cross-section is the difference between extinction and scattering cross-section

$$
C_{\text{abs}} = C_{\text{ext}} - C_{\text{sca}}.
\tag{6}
$$

To describe the nanoparticles' material, we consider a bulk permittivity of copper expressed as $\epsilon_{\exp}(\omega)$ but corrected by a term depending on the radius of the nanospheres to accommodate a size-dependent permittivity [47]. The size-dependent permittivity considers that additional scattering takes place of the electron density at the boundaries of the nanoparticles, which additionally acts as a damping to the charge density oscillations. The size-dependent permittivity can be stated as

$$
\epsilon(\omega) = \epsilon_{\exp}(\omega) + \frac{\omega_p^2}{\omega^2 + i\gamma_{\text{bulk}}\omega} - \frac{\omega_p^2}{\omega^2 + i\gamma\omega}
\tag{7}
$$

where the damping constant γ depends on the radius of the particle r, the damping constant of the bulk γ_{bulk}, the Fermi velocity v_F, and a constant A,

$$
\gamma = \gamma_{\text{bulk}} + \frac{Av_F}{r}.
\tag{8}
$$

The size of the particle affects the damping constant term in the permittivity so that the damping constant will get larger when the particle size is smaller. Detailed numbers for all the parameters can be found in the literature [47].

The optical response from each copper nanoparticle in alumina is represented in a dedicated T-matrix. In a second step, a global T-matrix is obtained that expresses the response from all 100 local nanoparticles considered to form the cluster. The global T-matrix, expressing the relation between the incident and scattered field for the entire cluster, is obtained through the translation theory of VSWF. This method assumes the addition theorem of VSWF [48] in local coordinates of each nanoparticle, creating a local T-matrix. A global T-matrix, which describes the scattering in a global coordinate system with its center of coordinate in the origin of the cluster, is defined as a matrix multiplication of a translation matrix and the local T-matrix [49].

After that, the global T-matrix, expressing the optical response from a cluster, is used in a multilayer periodic general Mie method code [49]. This code calculates the reflection and transmission of light from 2-dimensional lattices of periodically arranged scatterers. By using this method, assuming a linearly TM-polarized plane wave for the illumination, reflectance and transmittance from a thin-film consisting of the nanoparticles can be obtained. The thickness of this film is the cubical lattice constant of the unit cell. For example, the thickness of the layer is equal to 77.25 nm for the *FF* = 33.0% case depicted in Fig. 1.

However, the nanoparticle layer thickness cannot be varied easily when optimizing the absorber due to its dependency on the domain size of the cluster. Therefore, the nanoparticle layer is homogenized using the s-parameter retrieval method [50]. The effective material parameter, i.e., the complex permittivity, is calculated using the reflection coefficient *r* and transmission coefficient *t* data of the single thin-film in a vacuum with no substrate as

$$
\epsilon_{\text{eff}} = \frac{k_f}{\zeta_f},
\tag{9}
$$

where k_f and ζ_f are defined as

$$
\zeta_f = -k\sqrt{\frac{(r-1)^2 - t^2}{(r+1)^2 - t^2}},
\tag{10}
$$

and

$$
k_f = \left(-\cos^{-1}\left(\frac{1 - r^2 + t^2}{2t(1+r)} \right) + 2\pi m \right)\left(\frac{1}{d} \right),
\tag{11}
$$

where *k* is the wavenumber of the incoming field, m is the integer user-chosen branch order, and d is the thickness of the thin-film. For all practical reasons, the thin-films are such thin, that mostly we are in the lowest order branch. However, occasionally this needs to be adjusted.

Afterward, we construct a multilayer system composed of a film containing the copper nanoparticles, an alumina spacer layer, and the semi-infinite gold mirror, depicted in Fig. 2(a). The optical response from such a thin-film stack can be calculated using a standard thin-film transfer matrix algorithm [51]. The nanoparticles layer thickness (d_{np}) and the spacer layer thickness (d_{spacer}) are then swept to find the optimal absorptance curve in the spectral range between 250 nm and 1800 nm.

2.2. Experimental part

2.2.1. Synthesis of the absorber layer

All experiments are performed using a 2-in. RF magnetron (thin-films Consulting; Ionix) sputtering system with an alumina target and a separately attached custom-built gas aggregation source equipped with a custom build 2-in. magnetron with a Cu-target (99.99% purity). The GAS is connected to the main vacuum chamber via an exit orifice (3 mm diameter), while the RF magnetron sputtering system is connected with the main vacuum chamber (Fig. 2(a)). Between the RF magnetron sputtering system and the GAS is an angle of 45° (Fig. 2(b)). The main vacuum chamber is pumped by a turbo molecular pump (TMU 261, 210 L/s; Pfeiffer) and a dry scroll vacuum pump (nXDS10i; Edwards Vacuum). The argon gas is injected into the GAS through the magnetron, and the flow is controlled using a gas flow controller (1179BX22CM1BV with 200 sccm range; MKS Instruments Deutschland GmbH). The DC-power supply (M600DC-PS; Prevac) of the magnetron in the GAS is operated at 70 W for all experiments. The RF-power supply (VM 1000–1500; Dressler) of the RF magnetron is operated at 80 W (forward power 84 W, reflected power 4 W) for all experiments. The gas flow controller, the DC-power supply, and the RF-power supply are controlled via a computer. As a substrate, P-doped, (100)-oriented Si
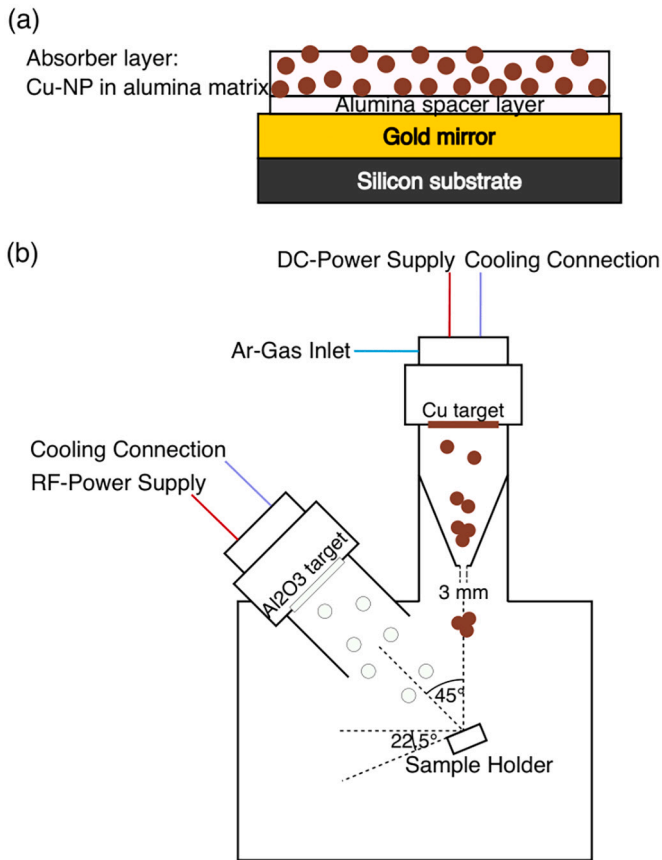
Fig. 2. (a) Schematic of the sample cross-section (not to scale). (b) Schematic of the experimental setup used for fabricating the samples.

wafers with native oxide (SiMat) are used. Before the deposition of the alumina, a 500 nm gold layer was deposited by magnetron sputtering onto the wafers using an additional adhesion promoter resulting in a flat gold film. The wafer is then cut into 10×10 mm² pieces.

For the absorber layer, firstly, a spacer layer of Al_2O_3 is deposited at an Ar-flow of 10 sccm resulting in a main chamber pressure of 2.5×10^{-3} mbar (base pressure 2.6×10^{-6} mbar). During the spacer deposition, the sample is turned to an angle of 45°. This results in normal orientation of the substrate to the alumina target. Afterward, the absorber layer containing copper nanoparticles in an Al_2O_3-matrix is deposited. Both materials are sputtered alternatingly at an Ar-flow of 40 sccm, resulting in a main chamber pressure of 5.5×10^{-3} mbar and a pressure inside the GAS of 2.1 mbar. Since there is an angle of 45° between the DC and RF magnetron, the sample is turned to a 22.5° angle between the alumina target and the exit orifice of the GAS (Fig. 2). One deposition cycle always consists of 30 s deposition of Cu NPs and a tunable deposition time of alumina t_{Al}. By adjusting the deposition time of the alumina matrix, the filling factor for each sample is adjusted. The deposition cycle is repeated until the desired film thickness is reached. For a filling factor of 0.33, the number of cycles was 80 and t_{Al} was 4.91 min, resulting in a deposition of 1 nm alumina per cycle. But for a filling factor of 0.415, the number of cycles increased to 128, while t_{Al} was reduced to 3.07 min. Despite the consecutive, step-wise character of the deposition process, the ballistic nature of the nanoparticle deposition and the relatively larger mean diameter of the nanoparticles (compared to the thickness of single-deposition-step Al_2O_3 layer) are expected to result efficiently in a random arrangement of nanoparticles in the nanocomposite.

Additionally, reference samples are prepared by depositing nanoparticles for 30s (without alumina) on a p-doped Si substrate using the process parameters used for the absorber layer. Such a sample is used to determine the size distribution by evaluating scanning electron microscope (SEM) micrographs. For each reference sample, micrographs are taken at five different locations and imageJ (vers. 1.53f51) is used to determine the size distribution of the deposited copper nanoparticles. At least 2000 particles are included in the experimental size distribution. The corresponding size distribution of nanoparticles, as depicted in Fig. 3(a), is considered in the simulations. Other parameters were tried, but the chosen ones are the best compromise between the different deposition rates of alumina and Cu-nanoparticles.

2.2.2. Film characterization

The reflection of the samples is measured with a spectroscopic ellipsometer (M2000-UI; J.A.Woollam), which is equipped with a Quartz Tungsten Halogen Deuterium lamp and a fixed polarizer. Therefore, the incident light is linearly polarized, and the spectral range goes from 245 nm to 1690 nm. The reflection is measured at the center of the sample at an angle of 60°. Film thickness is estimated from the recorded ellipsometer data using the analysis software CompleteEase (J. A.Woollam). Additionally, the film thickness is measured with a profilometer (Dektak XT, Bruker).

To determine the filling factor, EDX measurements are conducted. The EDX detector (Ultimax 65; Oxford instruments) is integrated into an SEM (Gemini Ultra55 Plus Microscope; Zeiss). For each nanocomposite absorber thin-film, EDX spectra were recorded at five different locations with an acceleration voltage of 15 kV. For a quantification of the obtained spectra, only the fraction of the elements copper (originating from the nanoparticles) and aluminum (originating from the dielectric matrix) are taken into account. From the estimated atomic fraction, the corresponding volume fractions can be approximated. First, the atomic fractions for Al and Cu are calculated as if Al and Cu are the only elements inside the sample as

$$x_{Al} = \frac{x_{Al}(EDX)}{x_{Al}(EDX) + x_{Cu}(EDX)}. \tag{12}$$

Since the spacer layer does not contain copper nanoparticles, the ratio between the volume of alumina inside the absorber layer and the total volume of alumina inside the sample is used to correct the atomic fraction of Al with a correction factor as

$$r_{Al} = \frac{V_{absorber}(Al_2O_3)}{V_{absorber}(Al_2O_3) + V_{spacer}}. \tag{13}$$

The volume fraction for alumina and the filling factor is then calculated as

$$FF = 1 - \phi_{Al_2O_3} = \frac{0.5 \cdot r_{Al} \cdot x_{Al} \cdot \frac{M_{Al_2O_3}}{\rho_{Al_2O_3}}}{0.5 \cdot r_{Al} \cdot x_{Al} \cdot \frac{M_{Al_2O_3}}{\rho_{Al_2O_3}} + x_{Cu} \cdot \frac{M_{Cu}}{\rho_{Cu}}} \tag{14}$$

The molar mass and density of alumina are 101.96 g mol⁻¹ and 2.97 g cm⁻³ [52], respectively, while the molar mass and density of copper are 63.55 g mol⁻¹ and 8.96 g cm⁻³, respectively.

3. Results and discussion

The nanoparticles' size distributions as measured and as used for the computations are depicted in Fig. 3. Please note, the measured size distribution contains information from >2000 nanoparticles which we could not consider in simulations. Therefore, the size distribution was down-sampled to only 100 nanoparticles preserving, nevertheless, the properties of the distribution. The probability density function of the experimental size distribution is extracted so that the down-sampling could be possible. Such distribution, nevertheless, is entirely sufficient to capture all the details of the size distribution, which makes it an adequate representation of the properties of the thin-film.

The absorber is characterized through a few independent degrees of freedom, such as the filling factor of the nanoparticles in the absorber
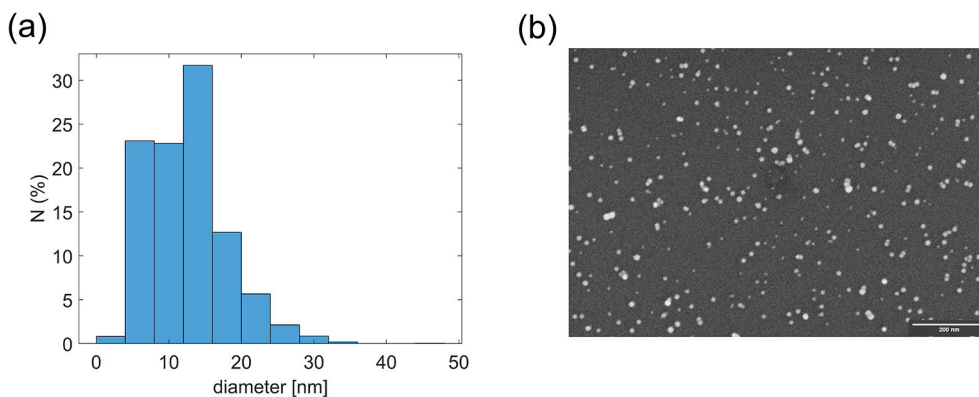
Fig. 3. (a) Nanoparticles size distribution for *FF* = 33.0% as measured. (b) SEM micrograph of Cu nanoparticles on Si substrate from which the size distribution is obtained.

layer and the thicknesses of each thin-film component. Moreover, the absorber can be operated at different incidence angles of illumination. We start by analyzing how the filling factor of the nanoparticles affects the absorption strength and broadens it. Some discrete filling factors are considered, i.e., *FF* = [23.0, 33.0, 41.5] %. A smaller filling factor of only 8.40% is also taken as an example to resemble nanoparticles that are generally not interacting with each other. We start the analysis by retrieving the complex effective permittivity (ϵ_{eff}) of all the films with the different filling factors and show them in Fig. 4. The spectra of the effective permittivity are characterized by a sequence of resonances that could be understood as a result of inter-particle interactions. These resonances can be explained through the plasmon hybridization model [38,39]. When a small-sized dimer interacts, the plasmons of the interacting particles are hybridized to form bonding and antibonding plasmons. The bonding plasmons are characterized by two dipole modes in-phase, and the antibonding plasmons are characterized by two dipole modes oscillating π-out-of-phase. When the interacting particles have small separations, the splitting between the bonding and antibonding plasmons can be recognized. The bonding mode will be supported at lower energy than the energy of the localized plasmon of the isolated nanosphere, and the antibonding mode will be supported at higher energy. According to Fig. 4, we believe that two promising resonances at longer wavelengths, i.e., at $\lambda \approx 800$ nm and $\lambda \approx 1000$ nm, in both the real and imaginary parts of ϵ_{eff} are mostly optically active bonding modes that result from the hybridization of plasmons from interacting nanoparticles in the layer. Here, the induced dipole moments are in-phase. These resonances at longer wavelengths redshift for higher filling factors (*FF* = 41.5%), being a further indication that they are linked to some

bonding modes. Also, it is known that the anti-bonding modes in the nanoparticles with spherical shape are hard to excite since that would require a pronounced gradient in the electric field across the spatial extent of the coupled nanoparticles. This is hard to achieve considering the small size of the nanoparticles and their rather dense packaging [53]. The resonance at $\lambda \approx 600$ nm that weakly redshifts for a higher filling factor is potentially linked to the localized surface plasmon resonance of the bare copper nanoparticles. The enhancement and the redshifting of the resonances when considering a higher filling factor can lead to stronger and broader absorption due to the emergence of localized electric field enhancement between the nanoparticles thanks to the plasmonic hybridization. From here, it is possible further tune the layer thicknesses and materials intrinsically to adjust the spectral position of the plasmonic resonance for maximizing the coupling between the nanoparticles. So, plasmonic hybridization plays an important role in our perfect absorber because the field enhancement caused by the hybridization at the closely-gap interacting nanoparticles can increase the absorption significantly. From a phenomenological point, it is a further degree of freedom that we can exploit to optimize the system in a suitable sense so that it maximizes our objective function.

As the filling factor increases, the resonance linked to the interaction of the particles at longer wavelengths ($\lambda > 1000$ nm) gets stronger, which can best be seen in the amplitude of the real and imaginary part of the effective permittivity that increases correspondingly. This means that energy losses within the layer could be stronger for a higher filling fraction. This leads to stronger and spectrally broader absorption at lower energies.

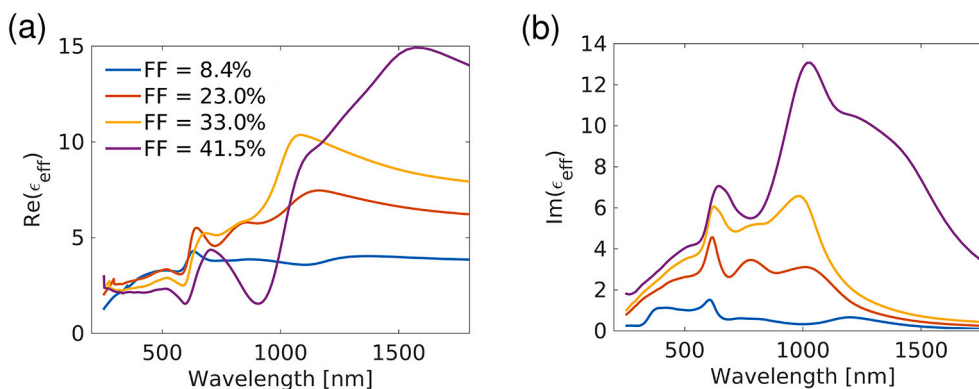Before we plot the absorbance from the thin-film, we need to know

Fig. 4. (a) Real and (b) imaginary part of the effective permittivity of thin-films made from Cu nanoparticles for different filling fractions in the spectral range from λ = 200–1800 nm.

whether the angle of incidence affects the absorption. To answer this question, we choose the thicknesses of the layers to be $d_{np} = 100$ nm and $d_{spacer} = 20$ nm. Transverse magnetic (TM) polarization is considered in this case at oblique incidence. We expect that there is an angle equivalent to Brewster's angle that causes the reflection to go to zero and hence maximizes the absorption. The effect of the incidence angle can be seen indeed in Fig. 5, where we plot the ratio of the integrated absorptance curve in the spectral range to the maximum possible absorptance curve across the relevant spectral domain from 250 nm until 1800 nm. This quantity is called the normalized area of absorptance ($area_A$) that has a value from 0 to 1. We see that Brewster's angle is consistently around $\theta = 60°$ for all variations of the filling fraction. Roughly, the normalized area is above 0.8 when the angle of incidence is approximately at $\theta = 0°$ - 70°, yet not perfect. Later, we consider the response at the normal incidence angle and the optimal angle of incidence, 60°.

Theoretically, zero reflection at the interface of the nanoparticle layer is possible as long as the generalized impedance of the overall thin-film layer stack is matched to that of air [30]. The destructive interference of the reflected light can be triggered by setting the proper intrinsic properties value of the layers to maximize the absorption, for example the nanoparticle layer thickness (d_{np}) and the alumina spacer layer thickness (d_{spacer}). Setting the spacer layer thickness is no less important to enhance the absorption [54–56]. So that, d_{np} and d_{spacer} are swept from 0 to 150 nm, and the normalized area of absorptance for all possible thickness combinations are calculated in this parameter range. Fig. 6 shows the colormap that explains the goodness of the absorption in a form of absorptance as a variation of the nanoparticle layer and the spacer layer thickness for filling fraction variation at normal incidence and the angle previously identified as Brewster's angle. It indicates that the absorption is maximal with a fairly thick nanoparticle layer and a thin spacer layer. In this parameter regime, the normalized area of absorptance above 0.9 is guaranteed for both angles of incidence and the considered filling fraction. The optimal thin-film thicknesses can be identified as long as they are on the optimal contour region. Although it is evident that thicker films result in a high absorption, we want to make sure that the optimal thickness is preferably as thin as possible, which is also convenient in the experimental point of view because thinner layers have the advantage of lower processing time, lower material costs and better compatibility with flexible substrates.

Finally, we consider the absorber configuration that is within the optimal contour region for the strongest broadband absorption of all the studied filling factor variations corresponding to Fig. 6 at Brewster's angle. We present the absorptance of a few selected absorber examples with various nanoparticle filling factors illuminated at Brewster's angle ($\theta = 60°$), according to Fig. 5. Exemplary, a thin-film absorber with $d_{np} = 80$ nm, $d_{spacer} = 13$ nm is considered. This configuration has been selected because the absorption is strong within our considered filling factor variations in general. The absorptance curves are depicted in
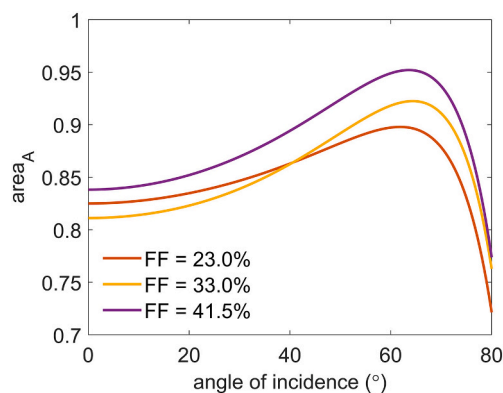
Fig. 7. According to these curves, almost perfect absorption at $\lambda = 250$ nm - 1200 nm can be reached when we consider an illumination close to the Brewster angle, where a normalized absorptance area above 0.9 was achieved. Strong and broadband absorption happens when the thin-film absorber has a relatively high filling factor with optimal thin-film thicknesses. At lower filling factors, we particularly notice a degradation in the absorptance at longer wavelengths. This points to the fact that mutual coupling between adjacent nanoparticles in denser samples, which shifts the collective boding mode to longer wavelengths, is decisive for the excellent performance.

The insights on optimal nanocomposite layer thickness and nanoparticle filling factor as well as spacer layer thickness are used to fabricate thin-film nanocomposite absorbers via a combination of nanoparticle beam deposition from GAS and RF sputter deposition. The fabricated multilayer thin-film absorbers containing the nanoparticle layer as depicted in Fig. 2(a) are considered. The fabricated samples have different nanoparticle layer thicknesses with different filling factors. The nanoparticle layer thickness is 114 nm for $FF = 33.0\%$ and 105 nm for $FF = 41.5\%$ with the alumina spacer layer thickness is consistent to 20 nm. According to Fig. 8, the experimentally measured absorptance is weaker than that simulated. However, the spectra contain many similar features, i.e., at $\lambda \approx 520$ nm and $\lambda \approx 950$ nm for $FF = 33.0\%$.

The deviation between the simulation and the fabricated sample can presumably be linked to different assumptions in the simulations, which cannot yet be fulfilled by the fabricated samples. The most crucial premise in the simulation is that the nanoparticles in the unit cell do not touch each other. Instead, they are close to each other to admit the coupling among their plasmon resonances, which finally leads to absorption in the IR range. But in the ideal case, as assumed in the simulation, the particles do never touch. However, nanoparticles produced with the GAS are randomly distributed on the sample surface, which makes the agglomeration of nanoparticles also possible [57]. In Fig. 9 (a), an SEM micrograph of Cu nanoparticles deposited onto a Si wafer after 30 s of deposition is shown. Some agglomerated particles are marked with red circles. We presume that there is no electromagnetic coupling between the touching particles, leading to less absorption. A simulation attempt has been made to confirm this hypothesis. We compare the absorption cross-section (C_{abs}) of a touching dimer and a non-touching dimer with a surface-to-surface gap distance of 1 nm. The absorption cross-section has been calculated using Eq. (6). The non-touching dimer has a higher absorption cross-section in general, except in $\lambda > 900$ nm, according to Fig. 9(b). The absorption in this wavelength range can be made stronger when more than two particles interact, leading to more complex electromagnetic coupling, as we have already discussed in the previous section. So, we can say that touching particles decrease absorption because the light trapping potential between the particles is lost.

Another assumption in the simulation is that the surface and the interfaces do not show roughness. In our case, however, the experimentally produced samples show roughness in Fig. 9(c). Large-sized nanoparticles deposited via beam deposition technique performed at room temperature can cause limited surface mobility at the surrounding dielectric matrix due to small surface diffusion at the substrate. This means that the deposition is not capable of fully smoothing the roughness that is introduced by the particles. Furthermore, the non-normal deposition can promote shadowing and hence enhance the roughness. Growth of the surface roughness at the experimental sample can disrupt the destructive interference between the interfaces of the absorber because the experimental absorber layer thickness is based on the computational absorption optimization in the first place. While for an isolated surface a rough interface can lead to stronger absorption when compared to the smooth surface [58], roughness is detrimental in these devices that sensitively exploit interference effects.
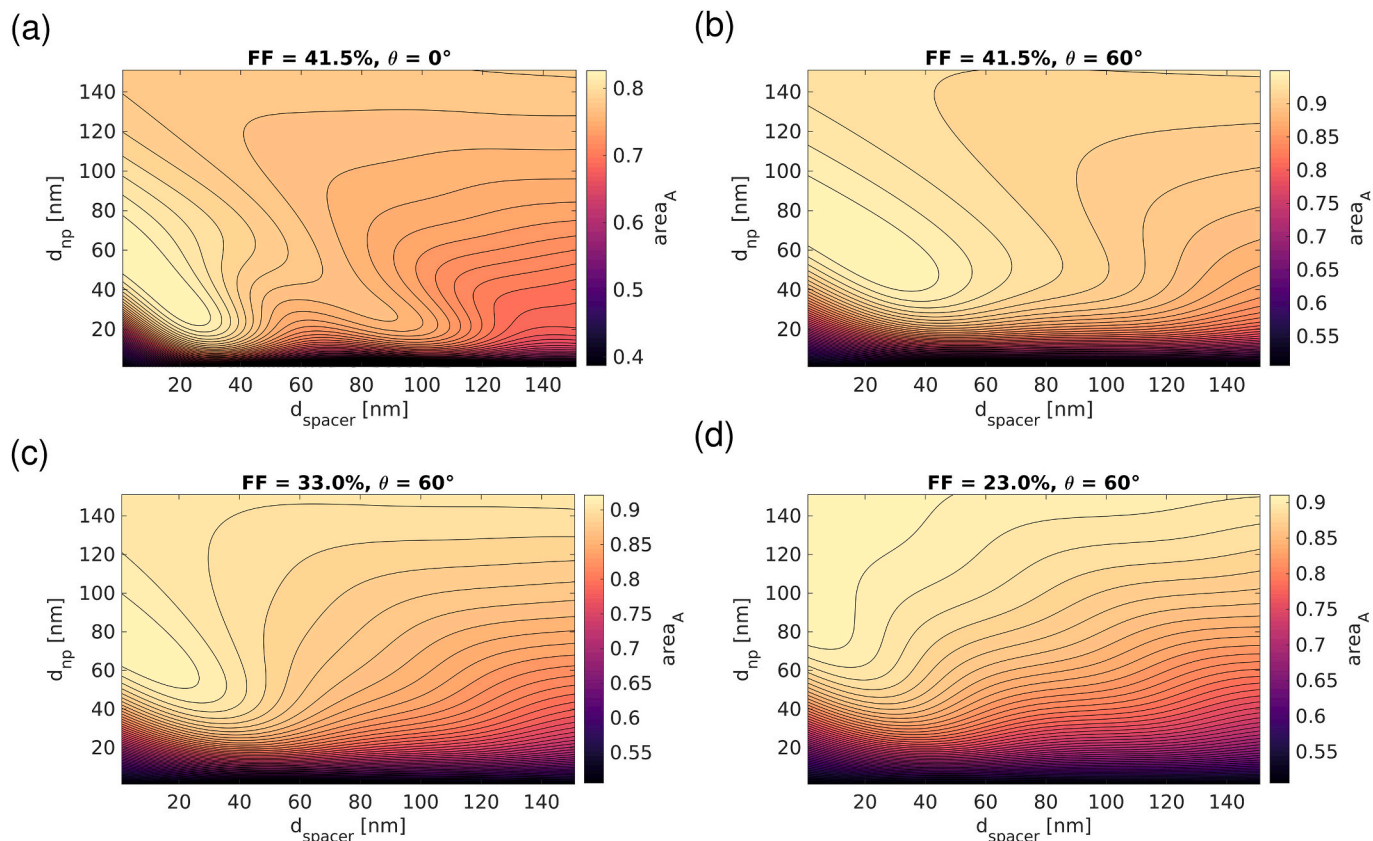

Fig. 5. Normalized area of absorptance as a function of the incidence angle for a TM polarized plane wave illumination and as a function of the filling fraction.

Fig. 6. The normalized area of absorptance in the broadband perfect absorber containing Cu nanoparticles at incidence angle (a) $\theta = 0°$ and (b) $\theta = 60°$ for filling fraction $FF = 41.5\%$ as a function of the layer thickness and the thickness of the spacer layer. Comparison to lower filling factor for (c) $FF = 33.0\%$ and (d) $FF = 23.0\%$ at $\theta = 60°$ are also depicted.
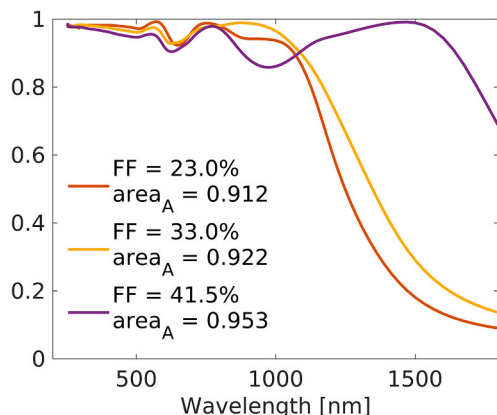

Fig. 7. Absorptance in a few selected examples where the thicknesses of the layers has been chosen at $d_{np} = 80$ nm, $d_{spacer} = 13$ nm. The absorptance is shown for three different filling fractions previously considered. The angles of incidence are chosen to be $\theta = 60°$.

4. Conclusions

We have studied a broadband thin-film-based perfect absorber using copper nanoparticles. Experimental and computational attempts have been made to analyze an absorber consisting of a copper nanoparticle layer in alumina, an alumina spacer layer, and a semi-infinite metallic mirror made of gold. By considering various nanoparticle filling factors, it was shown how absorptance can be computationally obtained using the T-matrix of a cluster of nanoparticles. Then, we optimize the

thicknesses of each component of the multilayer absorber to generate enough broad and strong absorption, especially at UV to near-infrared spectral ranges, using the fact that all reflected light can vanish if they have destructively interfered. The guiding design idea is always to consider on the one hand the directly reflected light at the first interface and the reflected light that experiences multiple round-trips in the layer stack. To achieve a suppressed reflection, these two components of the reflected light must have an identical amplitude and should be π-out-of-phase. Having a rather thin layer stack suppresses possible Fabry-Perot resonances and allows to achieve this effect in an extended spectral region. Eventually, the objective function is optimized while considering all degrees of freedom the system offers.

We found that using a more cost-friendly plasmonic material like copper in the alumina matrix, it is possible to have >90% of light energy absorbed by simulation in the considered polarization. We can say also that having a high filling factor of the nanoparticles is recommended for designing a thin-film based perfect absorber, though it is not trivial to determine the proper absorber layer thicknesses to maximize the absorption.

Based on the information obtained from the simulations, we fabricated and characterized dedicated devices. It turns out that the experimental absorptance curve yields weaker absorption strength, yet equivalent spectral features do appear compared to the computational result counterpart. Furthermore, the discrepancy in absorptance curve between the experimentally fabricated and simulated thin-film plasmonic absorbers is caused due to lack of interaction between the adjacent nanoparticles, and the emergence of surface roughness potentially led to weaker absorption in the experimental part.

It is encouraging that such thin absorber samples can be improved. The absorption at the NIR range, in particular, $\lambda > 1500$ nm, can be revamped by adding nanoparticles with material that sustain plasmon
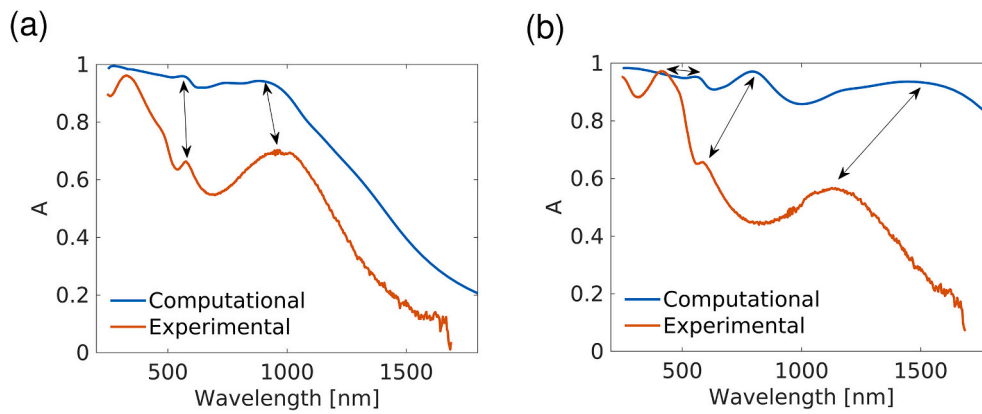
Fig. 8. Comparison of the simulation and experimental absorptance curves for two selected samples characterized by (a) FF = 33.0%, d_{np} = 114 nm and (b) FF = 41.5%, d_{np} =105 nm at d_{spacer} = 20 nm and for an incidence angle of 60°. The arrows act as a guide to the eye to highlight similar features between the experimental and numerical results.
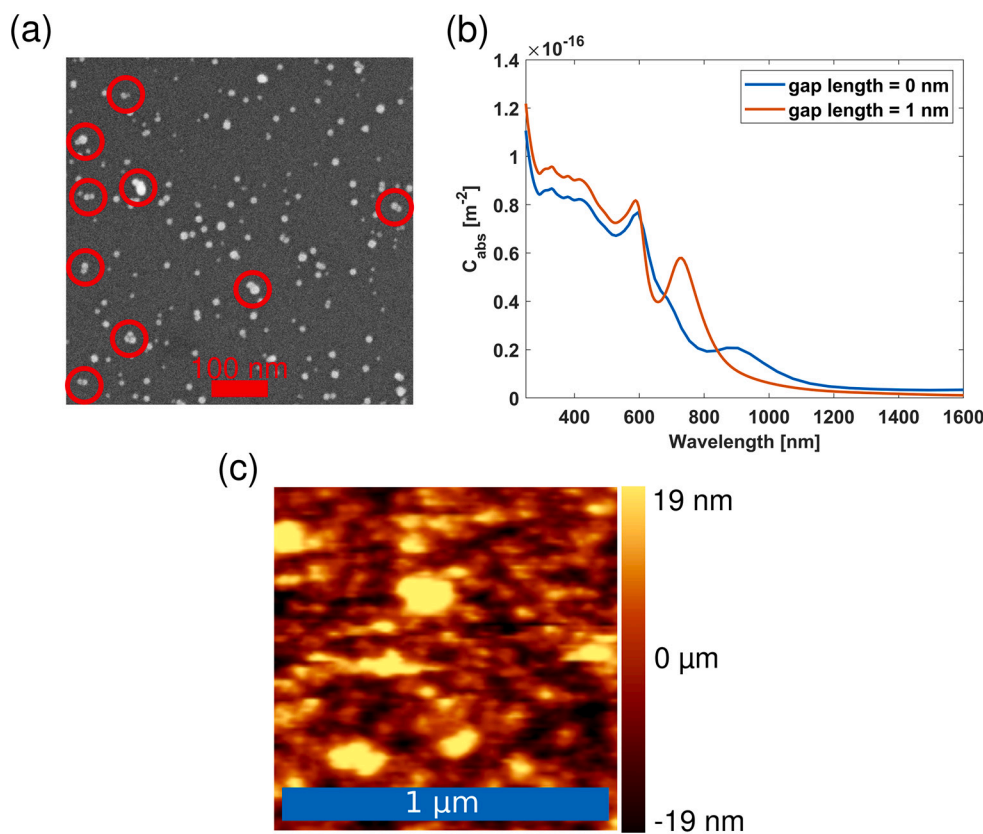

Fig. 9. (a) SEM picture after 30 s of copper nanoparticle deposition onto Si substrate. It is well visible that some nanoparticles are in touch with others. Some of them are marked with blue circles. (b) Absorption cross-section of touching and non-touching (gap separation =1 nm) copper dimer in alumina. (c) AFM topography color plot of an exemplary absorber layer structure with a total thickness of 47.1 nm is shown. The difference between the hills and valleys is 38 nm. This proves that the surface roughness can partially cause deviations between simulations and experiments. (For interpretation of the references to color in this figure legend, the reader is referred to the web version of this article.)

resonances at NIR wavelengths, for instance, ITO [59] or tungsten [60], and considering nanoparticles with shape variety because several papers have reported near-infrared plasmon resonances [61–63]. We believe that a much broader, stronger, and thinner absorber can be achieved by designing the absorber with nanoparticles that have broad plasmon resonances diversity.

Declaration of Competing Interest

The authors declare that they have no known competing financial interests or personal relationships that could have appeared to influence the work reported in this paper.

Acknowledgements

References

[1] R. Sauerborn, K. Ebi, Climate change and natural disasters: integrating science and practice to protect health, Glob. Health Action 5 (2012) 19295.

[2] R. Zell, Global climate change and the emergence/re-emergence of infectious diseases, Int. J. Med. Microbiol. 293 (2004) 16–26.

[3] N. Muellner, N. Arnold, K. Gufler, W. Kromp, W. Renneberg, W. Liebert, Nuclear energy - the solution to climate change? Energ Policy 155 (2021), 112363.

[4] M. Hoel, S. Kverndokk, Depletion of fossil fuels and the impacts of global warming, Resour. Energy Econ. 18 (2) (1996) 115–136.

[5] N. Novas, R.M. Garcia, J.M. Camacho, A. Alcayde, Advances in solar energy towards efficient and sustainable energy, Sustainability 13 (11) (2021) 6295.

[6] A. Steinfeld, Solar thermochemical production of hydrogen—a review, Sol. Energy 78 (5) (2005) 603–615.

[7] J.A. Duffie, W.A. Beckman, Design of Photovoltaic Systems, John Wiley & Sons, Ltd, 2013.

[8] G. Huang, S.R. Curt, K. Wang, C.N. Markides, Challenges and opportunities for nanomaterials in spectral splitting for high-performance hybrid solar photovoltaic-thermal applications: a review, Nano Mat. Sci. 2 (3) (2020) 183–203.

[9] G. Thuillier, M. Hersé, D. Labs, T. Foujols, W. Peetermans, D. Gillotay, P.C. Simon, H. Mandel, The solar spectral irradiance from 200 to 2400 nm as measured by the SOLSPEC spectrometer from the atlas and Eureca missions, Sol. Phys. 214 (1) (2003) 1–22.

[10] R.B. Pettit, R.R. Sowell, I.J. Hall, Black chrome solar selective coatings optimized for high temperature applications, Sol. Energy Mater. 7 (2) (1982) 153–170.

[11] B.X. Wang, L.L. Wang, G.Z. Wang, W.Q. Huang, X.F. Li, X. Zhai, Metamaterial-based low-conductivity alloy perfect absorber, J. Lightwave Technol. 32 (12) (2014) 2293–2298.

[12] J. Zhou, Z. Liu, G. Liu, P. Pan, X. Liu, C. Tang, Z. Liu, J. Wang, Ultra-broadband solar absorbers for high-efficiency thermophotovoltaics, Opt. Express 28 (24) (2020) 36476–36486.

[13] J. Li, Z. Chen, H. Yang, Z. Yi, X. Chen, W. Yao, T. Duan, P. Wu, G. Li, Y. Li, Tunable broadband solar energy absorber based on monolayer transition metal dichalcogenides materials using au nanocubes, Nanomaterials 10 (2) (2020) 257.

[14] H. Wang, L. Wang, Perfect selective metamaterial solar absorbers, Opt. Express 21 (S6) (2013) A1078–A1093.

[15] H. Cai, Y. Sun, X. Wang, S. Zhan, Design of an ultra-broadband near-perfect bilayer grating metamaterial absorber based on genetic algorithm, Opt. Express 28 (10) (2020) 15347–15359.

[16] V. Stelmakh, V. Rinnerbauer, R.D. Geil, P.R. Aimone, J.J. Senkevich, J. D. Joannopoulos, M. Soljačić, I. Celanovic, High-temperature tantalum tungsten alloy photonic crystals: stability, optical properties, and fabrication, Appl. Phys. Lett. 103 (12) (2013), 123903.

[17] M.G. Nielsen, A. Pors, O. Albrektsen, S.I. Bozhevolnyi, Efficient absorption of visible radiation by gap plasmon resonators, Opt. Express 20 (12) (2012) 13311–13319.

[18] R. Piao, D. Zhang, Ultra-broadband perfect absorber based on nanoarray of titanium nitride truncated pyramids for solar energy harvesting, Phys. E Low-Dimens. Syst. Nanostruct. 134 (2021), 114829.

[19] M.K. Hedayati, M. Javaherirahim, B. Mozooni, R. Abdelaziz, A. Tavassolizadeh, V. S.K. Chakravandhanula, V. Zaporojtchenko, T. Strunskus, F. Faupel, M. Elbahri, Design of a perfect black absorber at visible frequencies using plasmonic metamaterials, Adv. Mater. 23 (45) (2011) 5410–5414.

[20] M.K. Hedayati, A.U. Zillohu, T. Strunskus, F. Faupel, M. Elbahri, Plasmonic tunable metamaterial absorber as ultraviolet protection film, Appl. Phys. Lett. 104 (4) (2014).

[21] M.Z. Ghori, S. Veziroglu, A. Hinz, B.B. Shurtleff, O. Polonskyi, T. Strunskus, J. Adam, F. Faupel, O.C. Aktas, Role of UV plasmonics in the photocatalytic performance of TiO2 decorated with aluminum nanoparticles, ACS Appl. Nano Mater. 1 (8) (2018) 3760–3764.

[22] J. Ma, J. Wang, Z.-D. Hu, Z. Zhang, L. Pan, A. Di Falco, High-efficiency and ultrabroadband flexible absorbers based on transversely symmetrical multi-layer structures, AIP Adv. 9 (11) (2019), 115007.

[23] H. Peng, Y. Luo, X. Ying, Y. Pu, Y. Jiang, J. Xu, Z. Liu, Broadband and highly absorbing multilayer structure in mid-infrared, Appl. Opt. 55 (31) (2016) 8833–8838.

[24] M. Amin, M. Farhat, H. Baugci, An ultra-broadband multilayered graphene absorber, Opt. Express 21 (24) (2013) 29938–29948.

[25] X. Chen, H. Gong, S. Dai, D. Zhao, Y. Yang, Q. Li, M. Qiu, Near-infrared broadband absorber with film-coupled multilayer nanorods, Opt. Lett. 38 (13) (2013) 2247–2249.

[26] S. Mader, O.J.F. Martin, Mechanisms of perfect absorption in nano-composite systems, Opt. Express 26 (21) (2018) 27089–27100.

[27] M. Liu, M. Susli, D. Silva, G. Putrino, H. Kala, S. Fan, M. Cole, L. Faraone, V. P. Wallace, W.J. Padilla, D.A. Powell, I.V. Shadrivov, M. Martyniuk, Ultrathin tunable terahertz absorber based on MEMS-driven metamaterial, Microsyst. Nanoeng. 3 (1) (2017) 17033.

[28] S.P. Gaur, K. Rangra, D. Kumar, MEMS AlN pyroelectric infrared sensor with medium to long wave IR absorber, Sensors Actuators A Phys. 300 (2019), 111660.

[29] H. Hou, Q. Huang, G. Liu, G. Qiao, Enhanced performances of CMOS-MEMS thermopile infrared detectors using novel thin film stacks, Infrared Phys. Technol. 102 (2019), 103058.

[30] M.A. Kats, D. Sharma, J. Lin, P. Genevet, R. Blanchard, Z. Yang, M.M. Qazilbash, D. N. Basov, S. Ramanathan, F. Capasso, Ultra-thin perfect absorber employing a tunable phase change material, Appl. Phys. Lett. 101 (22) (2012), 221101.

[31] A. Cordaro, J. van de Groep, S. Raza, E.F. Pecora, F. Priolo, M.L. Brongersma, Antireflection high-index metasurfaces combining Mie and Fabry-Pérot resonances, ACS Photon. 6 (2) (2019) 453–459.

[32] Y.A. Akimov, W.S. Koh, Design of plasmonic nanoparticles for efficient subwavelength light trapping in thin-film solar cells, Plasmonics 6 (1) (2011) 155–161.

[33] S. Mokkapati, F.J. Beck, A. Polman, K.R. Catchpole, Designing periodic arrays of metal nanoparticles for light-trapping applications in solar cells, Appl. Phys. Lett. 95 (5) (2009) 53115.

[34] C. Hägglund, G. Zeltzer, R. Ruiz, A. Wangperawong, K.E. Roelofs, S.F. Bent, Strong coupling of plasmon and nanocavity modes for dual-band, near-perfect absorbers and ultrathin photovoltaics, ACS Photon. 3 (3) (2016) 456–463.

[35] J. Hao, H. Hao, J. Li, L. Shi, T. Zhong, C. Zhang, J. Dong, J. Xing, H. Liu, Z. Zhang, Light trapping effect in perovskite solar cells by the addition of Ag nanoparticles, using textured substrates, Nanomaterials 8 (10) (2018).

[36] P. Dhawan, M. Gaudig, A. Sprafke, R.B. Wehrspohn, C. Rockstuhl, Light-trapping structures for planar solar cells inspired by transformation optics, Opt. Express 29 (13) (2021) 19903–19919.

[37] G. Faraone, R. Modi, S. Marom, A. Podestà, M. Di Vece, Increasing the optical absorption in a-Si thin films by embedding gold nanoparticles, Opt. Mater. 75 (2018) 204–210.

[38] P. Nordlander, C. Oubre, E. Prodan, K. Li, M.I. Stockman, Plasmon hybridization in nanoparticle dimers, Nano Lett. 4 (5) (2004) 899–903.

[39] V. Myroshnychenko, J. Rodríguez-Fernández, I. Pastoriza-Santos, A.M. Funston, C. Novo, L.M. Liz-Marzán, F.J. Javier García de Abajo, Modelling the optical response of gold nanoparticles, Chem. Soc. Rev. 37 (9) (2008) 1792–1805.

[40] I. Fabijanić, V. Janicki, J. Ferré-Borrull, M. Bubaš, V. Blažek Bregović, L.F. Marsal, J. Sancho-Parramon, Plasmonic nanoparticles and island films for solar energy harvesting: a comparative study of Cu, Al, Ag and Au performance, Coatings 9 (6) (2019) 382.

[41] H. Haberland, M. Karrais, M. Mall, Y. Thurner, Thin films from energetic cluster impact: a feasibility study, J. Vac. Sci. Technol. A 10 (5) (1992) 3266–3271.

[42] A. Vahl, J. Strobel, W. Reichstein, O. Polonskyi, T. Strunskus, L. Kienle, F. Faupel, Single target sputter deposition of alloy nanoparticles with adjustable composition via a gas aggregation cluster source, Nanotechnology 28 (17) (2017), 175703.

[43] V. Baranau, U. Tallarek, Random-close packing limits for monodisperse and polydisperse hard spheres, Soft Matter 10 (21) (2014) 3826–3841.

[44] C. Bohren, D.R. Huffman, Absorption and Scattering of Light by Small Particles, Wiley Science Paperback Series, 1998.

[45] I. Fernandez-Corbaton, D. Beutel, C. Rockstuhl, A. Pausch, W. Klopper, Computation of electromagnetic properties of molecular ensembles, Chem. Phys. Chem. 21 (9) (2020) 878–887.

[46] M. Mischenko, L. Travis, A. Lacis, in: Scattering, Absorption,and Emission of Light by Small Particles, Cambridge University Press, 2002.

[47] T. Okamoto, Near-Field Spectral Analysis of Metallic Beads, Springer Berlin Heidelberg, Berlin, Heidelberg, 2001.

[48] Y.-L. Xu, Calculation of the addition coefficients in electromagnetic multisphere-scattering theory, J. Comput. Phys. 127 (2) (1996) 285–298.

[49] D. Beutel, A. Groner, C. Rockstuhl, I. Fernandez-Corbaton, Efficient simulation of biperiodic, layered structures based on the T-matrix method, J. Opt. Soc. Am. B 38 (6) (2021) 1782–1791.

[50] C. Menzel, C. Rockstuhl, T. Paul, F. Lederer, T. Pertsch, Retrieving effective parameters for metamaterials at oblique incidence, Phys. Rev. B - Condens. Matter Mater. Phys. 77 (19) (2008) 1–8.

[51] T.G. Mackay, A. Lakhtakia, The Transfer-Matrix Method in Electromagnetics and Optics, Morgan & Claypool Publishers, 2020.

[52] R.S. Nowicki, Properties of rf-sputtered Al2O3 films deposited by planar magnetron, J. Vac. Sci. Technol. 14 (1) (1977) 127–133.

[53] Q. Li, Z. Zhang, Bonding and anti-bonding modes of plasmon coupling effects in TiO2-Ag core-shell dimers, Sci. Rep. 6 (December 2015) (2016) 1–7.

[54] N.N. Lal, H. Zhou, M. Hawkeye, J.K. Sinha, P.N. Bartlett, G.A.J. Amaratunga, J. J Baumberg, Using spacer layers to control metal and semiconductor absorption in ultrathin solar cells with plasmonic substrates, Phys. Rev. B 85 (24) (2012), 245318.

[55] K. N'Konou, P. Torchio, Optical absorption enhancement by inserting ZnO optical spacer in plasmonic organic solar cells, J. Nanophoton. 12 (1) (2017) 12502.

[56] Q. Li, J. Lu, P. Gupta, M. Qiu, Engineering optical absorption in graphene and other 2D materials: advances and applications, Adv. Opt. Mat. 7 (20) (2019) 1900595.

[57] D. Nelli, M. Cerbelaud, R. Ferrando, C. Minnai, Tuning the coalescence degree in the growth of Pt–Pd nanoalloys, Nanoscale Adv. 3 (3) (2021) 836–846.

[58] J. Yu, C. Niu, T. Zhu, Y. Lv, Influence of surface morphology on absorptivity of light-absorbing materials, Int. J. Photoenergy 2019 (2019) 1476217.

[59] M. Kanehara, H. Koike, T. Yoshinaga, T. Teranishi, Indium tin oxide nanoparticles with compositionally tunable surface plasmon resonance frequencies in the near-IR region, J. Am. Chem. Soc. 131 (49) (2009) 17736–17737.

[60] J.U. Andersen, E. Bonderup, K. Hansen, Thermionic emission from clusters, J. Phys. B Atomic Mol. Phys. 35 (5) (2002) R1–R30.

[61] F. Qin, T. Zhao, R. Jiang, N. Jiang, Q. Ruan, J. Wang, L.-D. Sun, C.-H. Yan, H.-Q. Lin, Thickness control produces gold nanoplates with their plasmon in the visible and near-infrared regions, Adv. Opt. Mater. 4 (1) (2016) 76–85.

[62] N.K. Pathak, P.S. Kumar Parthasarathi, R.P. Sharma, Tuning of the surface plasmon resonance of aluminum nanoshell near-infrared regimes, Phys. Chem. Chem. Phys. 21 (18) (2019) 9441–9449.

[63] H. Jiang, J. Sabarinathan, Near infrared surface plasmon resonance of gold nanoring based plasmonic crystals for sensor applications, in: 2009 9th IEEE Conference on Nanotechnology (IEEE-NANO), 2009, pp. 777–780.